

Lepton flavor violating decays $\tau \rightarrow Pl$ in the $U(1)_X$ SSM model

Tong-Tong Wang^{1,2*}, Shu-Min Zhao^{1,2†}, Xing-Xing Dong^{1,2‡},

Lu-Hao Su^{1,2}, Ze-Ning Zhang^{1,2}, Wei Li^{1,2}, Tai-Fu Feng^{1,2,3}

¹ *Department of Physics, Hebei University, Baoding 071002, China*

² *Key Laboratory of High-precision Computation and Application of Quantum Field Theory of Hebei Province, Baoding 071002, China and*

³ *Department of Physics, Chongqing University, Chongqing 401331, China*

(Dated: November 10, 2021)

Abstract

$U(1)_X$ SSM is the extension of the minimal supersymmetric standard model(MSSM) and its local gauge group is $SU(3)_C \times SU(2)_L \times U(1)_Y \times U(1)_X$. To obtain this model, three singlet new Higgs superfields and right-handed neutrinos are added to MSSM. In the framework of $U(1)_X$ SSM, we study lepton flavor violating decays $\tau \rightarrow Pl (P = \pi, \eta, \eta'; l = \mu, e)$. According to the latest experimental data of $\tau \rightarrow Pe$ and $\tau \rightarrow P\mu$, the influence of different sensitive parameters on the results is analyzed to make a reasonable prediction for future experiments. From the numerical analysis, the non-diagonal elements which correspond to the generations of the initial lepton and final lepton are main sensitive parameters and lepton flavor violation(LFV) sources. This work can provide a basis for finding the existence of new physics(NP).

PACS numbers:

Keywords: lepton flavor violation, $U(1)_X$ SSM, new physics

* wtt961018@163.com

† zhaosm@hbu.edu.cn

‡ dxx_0403@163.com

I. INTRODUCTION

Neutrino oscillation experiment provides evidence of LFV[1]. In the standard model(SM), the branching ratio of lepton flavor violating process is depressed due to the very small neutrino mass, which is very difficult to be observed in current or future experiments[2]. However, for some new models based on the extension of the SM, the branching ratio of lepton flavor violating process is enhanced due to the introduction of new lepton flavor violating sources, which can be improved to the measurable range of the current experiment. Therefore, the study of LFV is very important to find NP.

We extend the MSSM with $U(1)$ local gauge group, whose symmetry group is $SU(3)_C \times SU(2)_L \times U(1)_Y \times U(1)_X$ [3–5]. It adds three Higgs singlet superfields and right-handed neutrino superfields beyond MSSM[6]. In this way, light neutrinos obtain tiny masses through the seesaw mechanism, which can explain the results of neutrino oscillation experiment. There are five neutral CP-even Higgs component fields in the model, which come from two Higgs doublets and three Higgs singlets respectively. Therefore, the mass mixing matrix is 5×5 , and the 125.1 GeV Higgs particle[7] corresponds to the lightest mass eigenstate. The little hierarchy problem in MSSM is relieved in $U(1)_X$ SSM by the right-handed neutrinos, sneutrinos and additional Higgs singlets. MSSM exists μ problem, while in the $U(1)_X$ SSM[8] this problem can be alleviated by the S field after vacuum spontaneous breaking.

To improve the corrections to LFV processes of $\tau \rightarrow Pl$, people extend SM in various ways. In the non-SUSY models including two Higgs doublet models[9, 10], littlest Higgs model with T parity[11], TC2 model[12], etc., there are a certain number of works for LFV processes. On the other hand, within SUSY models there are also some works for the LFV processes of $\tau \rightarrow Pl$. Some of the related SUSY models are MSSM[13, 14], supersymmetric seesaw mechanism model[15], R-parity violating SUSY[16]. The LFV decays $\tau \rightarrow Pl$ are also studied in the scenario of the minimal R-symmetric supersymmetric standard model. The effective field theory is used to study $\tau \rightarrow Pl$, and the Wilson coefficients of the LFV operators are restricted[17].

This work is to study the LFV of the $\tau \rightarrow Pl$ processes under the $U(1)_X$ SSM model. We deduce the relevant Feynman diagrams, numerically analyze the Feynman amplitude, decay width, and use the combination of random scattering and equal step search method to efficiently find reasonable parameter spaces. The effects of different reasonable parameter

spaces on the branching ratio $\text{Br}(\tau \rightarrow Pl)$ are compared. The latest observed upper limits on the LFV branching ratio of $\tau \rightarrow P\mu$ and $\tau \rightarrow Pe(P = \pi, \eta, \eta')$ at 90% confidence level (C.L.)[18] are

$$\begin{aligned} \text{Br}(\tau \rightarrow e\pi) &< 8.0 \times 10^{-8}, \quad \text{Br}(\tau \rightarrow e\eta) < 9.2 \times 10^{-8}, \quad \text{Br}(\tau \rightarrow e\eta') < 1.6 \times 10^{-7}, \\ \text{Br}(\tau \rightarrow \mu\pi) &< 1.1 \times 10^{-7}, \quad \text{Br}(\tau \rightarrow \mu\eta) < 6.5 \times 10^{-8}, \quad \text{Br}(\tau \rightarrow \mu\eta') < 1.3 \times 10^{-7}. \end{aligned} \quad (1)$$

The paper is organized as follows. In Sec.II, we mainly introduce the $U(1)_X\text{SSM}$ including its superpotential and the general soft breaking terms. In Sec.III, we give analytic expressions for the branching ratios of $\tau \rightarrow Pl$ decays in the $U(1)_X\text{SSM}$. In Sec.IV, we give the numerical analysis, and the summary is given in Sec.V. Finally, some mass matrices are collected in the Appendix.

II. THE $U(1)_X\text{SSM}$

As the $U(1)$ extension of MSSM, the local gauge group of $U(1)_X\text{SSM}$ is $SU(3)_C \otimes SU(2)_L \otimes U(1)_Y \otimes U(1)_X$ [19–21]. $U(1)_X\text{SSM}$ has new superfields such as three Higgs singlets $\hat{\eta}$, $\hat{\bar{\eta}}$, \hat{S} and right-handed neutrinos $\hat{\nu}_i$, which are beyond MSSM. Through the seesaw mechanism, light neutrinos obtain tiny mass at the tree level. The neutral CP-even parts of H_u , H_d , η , $\bar{\eta}$ and S mix together and form 5×5 mass squared matrix, whose lightest eigenvalue corresponds to the lightest CP-even Higgs mass. To get 125.1 GeV Higgs mass[22, 23], the loop corrections should be taken into account. The sneutrinos are disparted into CP-even sneutrinos and CP-odd sneutrinos, and their mass squared matrixes are both extended to 6×6 . In $U(1)_X\text{SSM}$, the concrete form of the superpotential is:

$$\begin{aligned} W = & l_W \hat{S} + \mu \hat{H}_u \hat{H}_d + M_S \hat{S} \hat{S} - Y_d \hat{d} \hat{q} \hat{H}_d - Y_e \hat{e} \hat{l} \hat{H}_d + \lambda_H \hat{S} \hat{H}_u \hat{H}_d \\ & + \lambda_C \hat{S} \hat{\eta} \hat{\bar{\eta}} + \frac{\kappa}{3} \hat{S} \hat{S} \hat{S} + Y_u \hat{u} \hat{q} \hat{H}_u + Y_X \hat{\nu} \hat{\eta} \hat{\bar{\nu}} + Y_\nu \hat{\nu} \hat{l} \hat{H}_u. \end{aligned} \quad (2)$$

We collect the explicit forms of two Higgs doublets and three Higgs singlets here

$$\begin{aligned} H_u &= \begin{pmatrix} H_u^+ \\ \frac{1}{\sqrt{2}}(v_u + H_u^0 + iP_u^0) \end{pmatrix}, & H_d &= \begin{pmatrix} \frac{1}{\sqrt{2}}(v_d + H_d^0 + iP_d^0) \\ H_d^- \end{pmatrix}, \\ \eta &= \frac{1}{\sqrt{2}}(v_\eta + \phi_\eta^0 + iP_\eta^0), & \bar{\eta} &= \frac{1}{\sqrt{2}}(v_{\bar{\eta}} + \phi_{\bar{\eta}}^0 + iP_{\bar{\eta}}^0), \\ S &= \frac{1}{\sqrt{2}}(v_S + \phi_S^0 + iP_S^0). \end{aligned} \quad (3)$$

TABLE I: The superfields in $U(1)_X$ SSM

Superfields	$SU(3)_C$	$SU(2)_L$	$U(1)_Y$	$U(1)_X$
\hat{Q}_i	3	2	1/6	0
\hat{u}_i^c	$\bar{3}$	1	-2/3	-1/2
\hat{d}_i^c	$\bar{3}$	1	1/3	1/2
\hat{L}_i	1	2	-1/2	0
\hat{e}_i^c	1	1	1	1/2
$\hat{\nu}_i$	1	1	0	-1/2
\hat{H}_u	1	2	1/2	1/2
\hat{H}_d	1	2	-1/2	-1/2
$\hat{\eta}$	1	1	0	-1
$\hat{\bar{\eta}}$	1	1	0	1
\hat{S}	1	1	0	0

The vacuum expectation values (VEVs) of the Higgs superfields H_u , H_d , η , $\bar{\eta}$ and S are denoted by v_u , v_d , v_η , $v_{\bar{\eta}}$ and v_S respectively. Two angles are defined as $\tan \beta = v_u/v_d$ and $\tan \beta_\eta = v_{\bar{\eta}}/v_\eta$.

The soft SUSY breaking terms of this model are shown as

$$\begin{aligned}
 \mathcal{L}_{soft} = & \mathcal{L}_{soft}^{MSSM} - B_S S^2 - L_S S - \frac{T_\kappa}{3} S^3 - T_{\lambda_C} S \eta \bar{\eta} + \epsilon_{ij} T_{\lambda_H} S H_d^i H_u^j \\
 & - T_X^{IJ} \bar{\eta} \tilde{\nu}_R^{I*} \tilde{\nu}_R^{*J} + \epsilon_{ij} T_\nu^{IJ} H_u^i \tilde{\nu}_R^{I*} \tilde{l}_j^J - m_\eta^2 |\eta|^2 - m_{\bar{\eta}}^2 |\bar{\eta}|^2 - m_S^2 S^2 \\
 & - (m_{\tilde{\nu}_R}^2)^{IJ} \tilde{\nu}_R^{I*} \tilde{\nu}_R^J - \frac{1}{2} \left(M_X \lambda_{\tilde{X}}^2 + 2 M_{BB'} \lambda_{\tilde{B}} \lambda_{\tilde{X}} \right) + h.c. \quad .
 \end{aligned} \tag{4}$$

The particle content and charge assignments for $U(1)_X$ SSM are shown in the Table I. In our previous work, we have proven that $U(1)_X$ SSM is anomaly free[20]. Different from MSSM, $U(1)_X$ SSM has a new effect called as the gauge kinetic mixing, which is produced from two Abelian groups $U(1)_Y$ and $U(1)_X$.

In general, the covariant derivatives of $U(1)_X$ SSM can be written as [24–27]

$$D_\mu = \partial_\mu - i \begin{pmatrix} Y & X \end{pmatrix} \begin{pmatrix} g_Y & g'_{YX} \\ g'_{XY} & g'_X \end{pmatrix} \begin{pmatrix} A_\mu^Y \\ A_\mu^X \end{pmatrix}, \tag{5}$$

with A_μ^Y and A_μ^X representing the gauge fields of $U(1)_Y$ and $U(1)_X$ respectively.

Based on the two unbroken Abelian gauge groups, we can perform the following operation [24, 26, 27]

$$\begin{pmatrix} g_Y & g'_{YX} \\ g'_{XY} & g'_X \end{pmatrix} R^T = \begin{pmatrix} g_1 & g_{YX} \\ 0 & g_X \end{pmatrix}, \quad (6)$$

here, R is the rotation matrix.

At the tree level, three neutral gauge bosons A_μ^X , A_μ^Y and V_μ^3 mix together, whose mass matrix is shown in the basis $(A_\mu^Y, V_\mu^3, A_\mu^X)[21]$

$$\begin{pmatrix} \frac{1}{8}g_1^2v^2 & -\frac{1}{8}g_1g_2v^2 & \frac{1}{8}g_1(g_{YX} + g_X)v^2 \\ -\frac{1}{8}g_1g_2v^2 & \frac{1}{8}g_2^2v^2 & -\frac{1}{8}g_2g_{YX}v^2 \\ \frac{1}{8}g_1(g_{YX} + g_X)v^2 & -\frac{1}{8}g_2(g_{YX} + g_X)v^2 & \frac{1}{8}(g_{YX} + g_X)^2v^2 + \frac{1}{8}g_X^2\xi^2 \end{pmatrix}, \quad (7)$$

with $v^2 = v_u^2 + v_d^2$ and $\xi^2 = v_\eta^2 + v_{\bar{\eta}}^2$.

To get mass eigenvalues of the matrix in Eq.(7), we use two mixing angles θ_W and θ'_W . θ_W is the Weinberg angle and the new mixing angle θ'_W is defined from the following formula $\sin^2 \theta'_W = \frac{1}{2} - \frac{[(g_{YX} + g_X)^2 - g_1^2 - g_2^2]v^2 + 4g_X^2\xi^2}{2\sqrt{[(g_{YX} + g_X)^2 + g_1^2 + g_2^2]v^4 + 8g_X^2[(g_{YX} + g_X)^2 - g_1^2 - g_2^2]v^2\xi^2 + 16g_X^4\xi^4}}$ (8) It appears in the couplings involving Z and Z' . The exact eigenvalues of Eq. (7) are deduced [21]

$$\begin{aligned} m_\gamma^2 &= 0, \\ m_{Z,Z'}^2 &= \frac{1}{8} \left([g_1^2 + g_2^2 + (g_{YX} + g_X)^2]v^2 + 4g_X^2\xi^2 \right. \\ &\quad \left. \mp \sqrt{[g_1^2 + g_2^2 + (g_{YX} + g_X)^2]v^4 + 8[(g_{YX} + g_X)^2 - g_1^2 - g_2^2]g_X^2v^2\xi^2 + 16g_X^4\xi^4} \right). \end{aligned} \quad (9)$$

The mass squared matrix for CP-even sneutrino (ϕ_l, ϕ_r) reads

$$M_{\nu R}^2 = \begin{pmatrix} m_{\phi_l \phi_l} & m_{\phi_r \phi_l}^T \\ m_{\phi_l \phi_r} & m_{\phi_r \phi_r} \end{pmatrix}, \quad (10)$$

$$\begin{aligned} m_{\phi_l \phi_l} &= \frac{1}{8} \left((g_1^2 + g_{YX}^2 + g_2^2 + g_{YX}g_X)(v_d^2 - v_u^2) + g_{YX}g_X(2v_\eta^2 - 2v_{\bar{\eta}}^2) \right) \\ &\quad + \frac{1}{2}v_u^2 Y_\nu^T Y_\nu + M_L^2, \end{aligned} \quad (11)$$

$$m_{\phi_l \phi_r} = \frac{1}{\sqrt{2}}v_u T_\nu + v_u v_{\bar{\eta}} Y_X Y_\nu - \frac{1}{2}v_d(\lambda_H v_S + \sqrt{2}\mu)Y_\nu, \quad (12)$$

$$\begin{aligned} m_{\phi_r \phi_r} &= \frac{1}{8} \left((g_{YX}g_X + g_X^2)(v_d^2 - v_u^2) + 2g_X^2(v_\eta^2 - v_{\bar{\eta}}^2) \right) + v_\eta v_S Y_X \lambda_C \\ &\quad + M_\nu^2 + \frac{1}{2}v_u^2 |Y_\nu|^2 + v_{\bar{\eta}}(2v_{\bar{\eta}} Y_X Y_X + \sqrt{2}T_X). \end{aligned} \quad (13)$$

The matrix Z^R is used to diagonalize $M_{\tilde{\nu}^R}^2$. We also deduce the mass squared matrix for CP-odd sneutrino (σ_l, σ_r) and use the matrix Z^I to diagonalize it,

$$M_{\tilde{\nu}^I}^2 = \begin{pmatrix} m_{\sigma_l \sigma_l} & m_{\sigma_r \sigma_l}^T \\ m_{\sigma_l \sigma_r} & m_{\sigma_r \sigma_r} \end{pmatrix}, \quad (14)$$

$$m_{\sigma_l \sigma_l} = \frac{1}{8} \left((g_1^2 + g_{YX}^2 + g_2^2 + g_{YX} g_X)(v_d^2 - v_u^2) + 2g_{YX} g_X(v_\eta^2 - v_{\bar{\eta}}^2) \right) + \frac{1}{2} v_u^2 Y_\nu^T Y_\nu + M_{\tilde{L}}^2, \quad (15)$$

$$m_{\sigma_l \sigma_r} = \frac{1}{\sqrt{2}} v_u T_\nu - v_u v_{\bar{\eta}} Y_X Y_\nu - \frac{1}{2} v_d (\lambda_H v_S + \sqrt{2} \mu) Y_\nu, \quad (16)$$

$$m_{\sigma_r \sigma_r} = \frac{1}{8} \left((g_{YX} g_X + g_X^2)(v_d^2 - v_u^2) + 2g_X^2(v_\eta^2 - v_{\bar{\eta}}^2) \right) - v_\eta v_S Y_X \lambda_C + M_{\tilde{\nu}}^2 + \frac{1}{2} v_u^2 |Y_\nu|^2 + v_{\bar{\eta}} (2v_{\bar{\eta}} Y_X Y_X - \sqrt{2} T_X). \quad (17)$$

One can find other mass matrixes in the Appendix and Ref.[19].

Here, we show some needed couplings in this model. The charginos interact with down-quarks and up-squarks

$$\mathcal{L}_{\chi^- \bar{u} d} = \bar{\chi}_i^- \left((V_{i2}^* Y_u^j Z_{k,3+j}^U - g_2 V_{i1}^* Z_{kj}^U) P_L + Y_d^{j*} Z_{k,b}^U U_{i2} P_R \right) d_j \tilde{u}_k^*, \quad (18)$$

We also deduce the vertexes of $Z - \tilde{e}_i - \tilde{e}_j^*$

$$\begin{aligned} \mathcal{L}_{Z \tilde{e} \tilde{e}^*} = & \frac{1}{2} \tilde{e}_j^* \left[(g_2 \cos \theta_W \cos \theta'_W - g_1 \cos \theta'_W \sin \theta_W + g_{YX} \sin \theta'_W) \sum_{a=1}^3 Z_{i,a}^{E,*} Z_{j,a}^E \right. \\ & \left. + \left((2g_{YX} + g_X) \sin \theta'_W - 2g_1 \cos \theta'_W \sin \theta_W \right) \sum_{a=1}^3 Z_{i,3+a}^{E,*} Z_{j,3+a}^E \right] (p_i^\mu - p_j^\mu) \tilde{e}_i Z_\mu. \end{aligned} \quad (19)$$

To save space in the text, the remaining vertexes can be found in Refs.[20, 21, 28, 29].

III. FORMULATION

At the quark level, the effective Lagrangian for $\tau \rightarrow Pl$ can be written as[30]

$$\begin{aligned} \mathcal{L}_{\tau \rightarrow Pl} = & X_{LL}^I (\bar{l}_\alpha P_L \tau) (\bar{d} P_L d) + Y_{LL}^I (\bar{l}_\alpha P_L \tau) (\bar{u} P_L u) \\ & + X_{LR}^I (\bar{l}_\alpha P_L \tau) (\bar{d} P_R d) + Y_{LR}^I (\bar{l}_\alpha P_L \tau) (\bar{u} P_R u) \\ & + X_{LL}^J (\bar{l}_\alpha \gamma_\mu P_L \tau) (\bar{d} \gamma^\mu P_L d) + Y_{LL}^J (\bar{l}_\alpha \gamma_\mu P_L \tau) (\bar{u} \gamma^\mu P_L u) \\ & + X_{LR}^J (\bar{l}_\alpha \gamma_\mu P_L \tau) (\bar{d} \gamma^\mu P_R d) + Y_{LR}^J (\bar{l}_\alpha \gamma_\mu P_L \tau) (\bar{u} \gamma^\mu P_R u) + (L \leftrightarrow R) + h.c., \end{aligned} \quad (20)$$

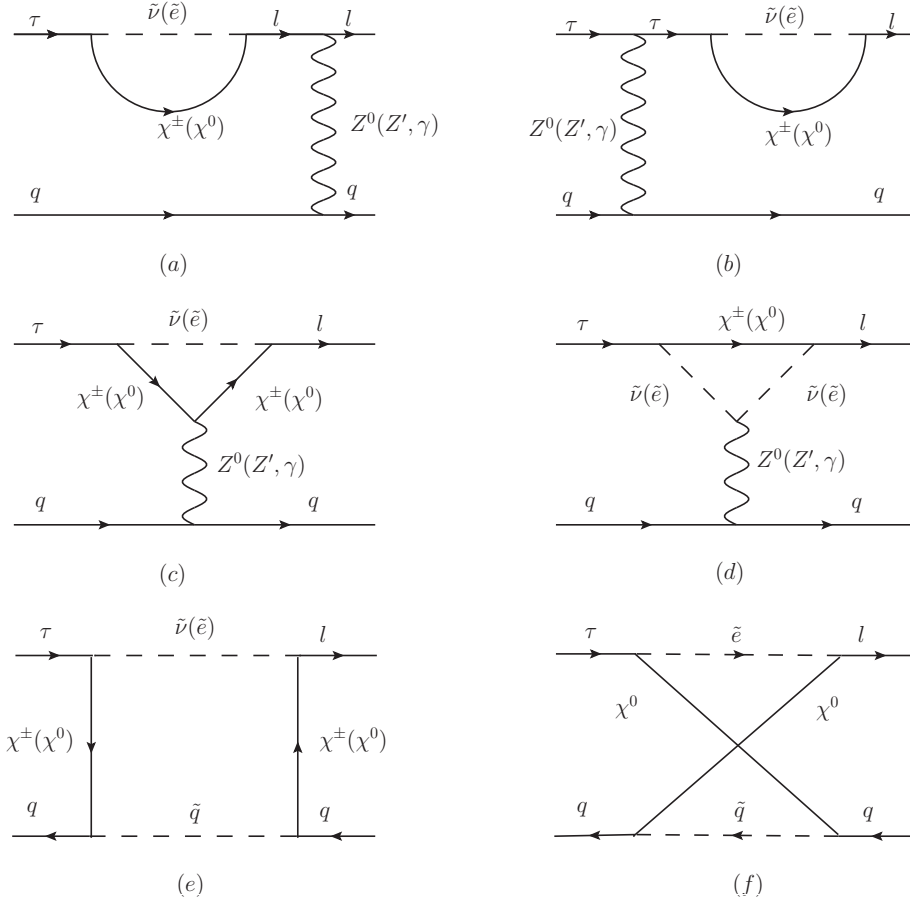


FIG. 1: The Feynman diagrams contributing to $\tau \rightarrow Pl$ in the $U(1)_X$ SSM. There are three types of diagrams: self-energy diagrams (a) and (b), penguin diagrams (c) and (d), box diagrams (e) and (f).

where the index $\alpha (= 1, 2)$ denotes the generation of the emitted lepton and $l_1(l_2) = e(\mu)$.

We show the studied Feynman diagrams contributing to $\tau \rightarrow Pl$ in the Fig.1. Taking Fig.1(c) as an example, the effective amplitude can be written as

$$\begin{aligned}
\mathcal{M}_{(c)} = & \sum_{\tilde{\nu}=\tilde{\nu}^I, \tilde{\nu}^R} \left[- \left(\frac{1}{2m_Z^2} G_3(x_{\tilde{\nu}}, x_{\chi^\pm}) A_R^{\tilde{\nu} \bar{l}_i \chi^\pm} B_R^{\bar{\chi}^\pm Z^0 \chi^\pm} C_L^{\tilde{\nu} \bar{\chi}^\pm \tau} D_L^{\bar{q} Z^0 q} \right. \right. \\
& + \frac{x_f}{m_Z^2} I_3(x_{\tilde{\nu}}, x_{\chi^\pm}) A_R^{\tilde{\nu} \bar{l}_i \chi^\pm} B_L^{\bar{\chi}^\pm Z^0 \chi^\pm} C_L^{\tilde{\nu} \bar{\chi}^\pm \tau} D_L^{\bar{q} Z^0 q} \left. \right) (\bar{l}_i \gamma^\mu P_L \tau) (\bar{q} \gamma_\mu P_L q) \\
& - \left(\frac{1}{2m_Z^2} G_3(x_{\tilde{\nu}}, x_{\chi^\pm}) A_L^{\tilde{\nu} \bar{l}_i \chi^\pm} B_L^{\bar{\chi}^\pm Z^0 \chi^\pm} C_R^{\tilde{\nu} \bar{\chi}^\pm \tau} D_L^{\bar{q} Z^0 q} \right. \\
& + \frac{x_f}{m_Z^2} I_3(x_{\tilde{\nu}}, x_{\chi^\pm}) A_L^{\tilde{\nu} \bar{l}_i \chi^\pm} B_R^{\bar{\chi}^\pm Z^0 \chi^\pm} C_R^{\tilde{\nu} \bar{\chi}^\pm \tau} D_L^{\bar{q} Z^0 q} \left. \right) (\bar{l}_i \gamma^\mu P_R \tau) (\bar{q} \gamma_\mu P_L q) \\
& - \left(\frac{1}{2m_Z^2} G_3(x_{\tilde{\nu}}, x_{\chi^\pm}) A_R^{\tilde{\nu} \bar{l}_i \chi^\pm} B_R^{\bar{\chi}^\pm Z^0 \chi^\pm} C_L^{\tilde{\nu} \bar{\chi}^\pm \tau} D_R^{\bar{q} Z^0 q} \right.
\end{aligned}$$

$$\begin{aligned}
& + \frac{x_f}{m_Z^2} I_3(x_{\bar{\nu}}, x_{\chi^\pm}) A_R^{\bar{\nu} l_i \chi^\pm} B_L^{\bar{\chi}^\pm Z^0 \chi^\pm} C_L^{\bar{\nu} \bar{\chi}^\pm \tau} D_R^{\bar{q} Z^0 q} (\bar{l}_i \gamma^u P_L \tau) (\bar{q} \gamma_u P_R q) \\
& - \left(\frac{1}{2m_Z^2} G_3(x_{\bar{\nu}}, x_{\chi^\pm}) A_L^{\bar{\nu} l_i \chi^\pm} B_L^{\bar{\chi}^\pm Z^0 \chi^\pm} C_R^{\bar{\nu} \bar{\chi}^\pm \tau} D_R^{\bar{q} Z^0 q} \right. \\
& \left. + \frac{x_f}{m_Z^2} I_3(x_{\bar{\nu}}, x_{\chi^\pm}) A_L^{\bar{\nu} l_i \chi^\pm} B_R^{\bar{\chi}^\pm Z^0 \chi^\pm} C_R^{\bar{\nu} \bar{\chi}^\pm \tau} D_R^{\bar{q} Z^0 q} \right) (\bar{l}_i \gamma^u P_R \tau) (\bar{q} \gamma_u P_R q) \Big], \quad (21)
\end{aligned}$$

where $x_i = m_i^2/m_W^2$. The functions $G_3(x_1, x_2)$ and $I_3(x_1, x_2)$ are

$$\begin{aligned}
G_3(x_1, x_2) &= \frac{1}{16\pi^2} \left[1 + \ln x_\mu + \frac{x_2^2 \ln x_2 - x_1^2 \ln x_1}{(x_2 - x_1)^2} + \frac{x_2 + 2x_2 \ln x_2}{x_1 - x_2} \right], \\
I_3(x_1, x_2) &= \frac{1}{16\pi^2} \left[\frac{1 + \ln x_2}{x_2 - x_1} + \frac{x_1 \ln x_1 - x_2 \ln x_2}{(x_2 - x_1)^2} \right]. \quad (22)
\end{aligned}$$

A, B, C, D are coupling constants of the corresponding vertexes, whose concrete forms can be found in Refs.[20, 21, 28].

The coefficients $c_P^{I,J}$ and $d_P^{I,J}$ are liner combinations of the Wilson coefficients in the interaction Lagrangian for $\tau \rightarrow Pl$ [17]

$$\begin{aligned}
c_P^I &= \frac{f_\pi}{2} \left[\frac{D_L^d(P)}{m_d} (X_{LL}^I + X_{RL}^I) + \frac{D_L^u(P)}{m_u} (Y_{LL}^I + Y_{RL}^I) \right. \\
& \quad \left. + \frac{D_R^d(P)}{m_d} (X_{LR}^I + X_{RR}^I) + \frac{D_R^u(P)}{m_u} (Y_{LR}^I + Y_{RR}^I) \right], \\
d_P^I &= \frac{f_\pi}{2} \left[\frac{D_L^d(P)}{m_d} (X_{RL}^I - X_{LL}^I) + \frac{D_L^u(P)}{m_u} (Y_{RL}^I - Y_{LL}^I) \right. \\
& \quad \left. + \frac{D_R^d(P)}{m_d} (X_{RR}^I - X_{LR}^I) + \frac{D_R^u(P)}{m_u} (Y_{RR}^I - Y_{LR}^I) \right], \\
c_P^J &= \frac{f_\pi}{4} C(P) (m_\pi - m_l) [X_{LR}^J - X_{LL}^J - X_{RL}^J + X_{RR}^J + Y_{LL}^J - Y_{LR}^J + Y_{RL}^J - Y_{RR}^J], \\
d_P^J &= \frac{f_\pi}{4} C(P) (m_\pi + m_l) [X_{LR}^J - X_{LL}^J + X_{RL}^J - X_{RR}^J + Y_{LL}^J - Y_{LR}^J - Y_{RL}^J + Y_{RR}^J]. \quad (23)
\end{aligned}$$

The expressions for coefficients $C(P), D_L^{d,u}(P)$ are listed in Table II. Here, m_π and m_K denote the masses of neutral pion and Kaon, and θ_η denotes the $\eta \rightarrow \eta'$ mixing angle. In addition, $D_R^{d,u}(P) = -(D_L^{d,u}(P))^*$ and f_π is the pion decay constant.

The averaged squared amplitude can be written as

$$\begin{aligned}
|\mathcal{M}|^2 &= 2m_\tau m_l (c_P^I c_P^{I*} - d_P^I d_P^{I*}) + (m_\tau^2 + m_l^2 - m_P^2) (c_P^I c_P^{I*} + d_P^I d_P^{I*}) \\
& \quad + 2m_\tau m_l (c_P^J c_P^{J*} - d_P^J d_P^{J*}) + (m_\tau^2 + m_l^2 - m_P^2) (c_P^J c_P^{J*} + d_P^J d_P^{J*}) \\
& \quad + 2m_\tau m_l (c_P^I c_P^{J*} - d_P^I d_P^{J*}) + (m_\tau^2 + m_l^2 - m_P^2) (c_P^I c_P^{J*} + d_P^I d_P^{J*}) \\
& \quad + 2m_\tau m_l (c_P^J c_P^{I*} - d_P^J d_P^{I*}) + (m_\tau^2 + m_l^2 - m_P^2) (c_P^J c_P^{I*} + d_P^J d_P^{I*}). \quad (24)
\end{aligned}$$

TABLE II: Coefficients for each pseudoscalar meson P [31]

	$C(P)$	$D_L^d(P)$	$D_L^u(P)$
$P = \pi$	1	$-\frac{m_\pi^2}{4}$	$\frac{m_\pi^2}{4}$
$P = \eta$	$\frac{1}{\sqrt{6}}(\sin \theta_\eta + \sqrt{2} \cos \theta_\eta)$	$\frac{1}{4\sqrt{3}}[(3m_\pi^2 - 4m_K^2) \cos \theta_\eta - 2\sqrt{2}m_K^2 \sin \theta_\eta]$	$\frac{1}{4\sqrt{3}}m_\pi^2(\cos \theta_\eta - \sqrt{2} \sin \theta_\eta)$
$P = \eta'$	$\frac{1}{\sqrt{6}}(\sqrt{2} \sin \theta_\eta - \cos \theta_\eta)$	$\frac{1}{4\sqrt{3}}[(3m_\pi^2 - 4m_K^2) \sin \theta_\eta + 2\sqrt{2}m_K^2 \cos \theta_\eta]$	$\frac{1}{4\sqrt{3}}m_\pi^2(\sin \theta_\eta + \sqrt{2} \cos \theta_\eta)$

Then the decay width for $\tau \rightarrow Pl$ is given by

$$\Gamma(\tau \rightarrow Pl) = \frac{\lambda^{1/2}(m_\tau^2, m_l^2, m_P^2)}{16\pi m_\tau^3} \sum_{i,f} |\mathcal{M}|^2. \quad (25)$$

The beanching ratio of $\tau \rightarrow Pl$ is

$$Br(\tau \rightarrow Pl) = \Gamma(\tau \rightarrow Pl)/\Gamma_\tau, \quad (26)$$

here $\Gamma_\tau \simeq 2.266 \times 10^{-12}$ GeV, Γ_τ is the total width of τ [20].

IV. NUMERICAL RESULTS

In this section, we study the numerical results. The lightest CP-even Higgs mass $m_{h^0}=125.1$ GeV[32, 33] is considered. For the mass of the added heavy vector boson Z' , the latest constraint from experiment is $M_{Z'} > 5.1$ TeV[34], which is heavier than the former constraints. The upper bound on the ratio between $M_{Z'}$ and its gauge coupling g_X is $M_{Z'}/g_X \geq 6$ TeV at 99% C.L.[35, 36]. Taking into account the constraint from LHC data, $\tan \beta_\eta < 1.5$ [37]. We also consider the limits for the masses of the particles beyond SM, which include neutralino, chargino, scalar neutrino, scalar lepton, scalar quark and so on. Since $M_{Z'}$ is much larger than M_Z , the contribution of Z' is very small at the amplitude level, so we won't calculate it here.

Considering the above constraints in the front paragraph, we use the following parameters

$$\begin{aligned}
 &M_S = 2.7 \text{ TeV}, \quad T_\kappa = 1.6 \text{ TeV}, \quad M_1 = 1.2 \text{ TeV}, \quad M_{BL} = 1 \text{ TeV}, \quad g_{YX} = 0.2, \\
 &\xi = 15.5 \text{ TeV}, \quad Y_{X11} = Y_{X22} = 0.5, \quad Y_{X33} = 0.4, \quad g_X = 0.33, \quad \kappa = 1, \quad \lambda_C = -0.08, \\
 &M_{BB'} = 0.4 \text{ TeV}, \quad T_{\lambda_H} = 0.3 \text{ TeV}, \quad T_{X11} = T_{X22} = T_{X33} = -1 \text{ TeV}, \quad l_W = 4 \text{ TeV}^2, \\
 &\lambda_H = 0.1, \quad T_{e11} = T_{e22} = T_{e33} = -3 \text{ TeV}, \quad \tan \beta_\eta = 0.8, \quad B_\mu = B_S = 1 \text{ TeV}^2, \\
 &T_{\lambda_C} = -0.1 \text{ TeV}, \quad \mu = 0.5 \text{ TeV}, \quad M_{\tilde{E}11}^2 = M_{\tilde{E}22}^2 = M_{\tilde{E}33}^2 = 3.54 \text{ TeV}^2.
 \end{aligned} \quad (27)$$

To simplify the numerical research, we use the relations for the parameters and they vary in the following numerical analysis

$$\begin{aligned}
M_{\nu 11}^2 &= M_{\nu 22}^2 = M_{\nu 33}^2 = m_\nu^2, \quad M_{L 11}^2 = M_{L 22}^2 = M_{L 33}^2 = m_L^2, \\
T_{\nu 11} &= T_{\nu 22} = T_{\nu 33} = T_\nu, \quad M_{L 12}^2 = M_{L 21}^2, \quad M_{L 13}^2 = M_{L 31}^2, \\
M_{L 32}^2 &= M_{L 23}^2, \quad M_{\nu 12}^2 = M_{\nu 21}^2, \quad M_{\nu 13}^2 = M_{\nu 31}^2, \quad M_{\nu 23}^2 = M_{\nu 32}^2, \\
T_{e 12} &= T_{e 21}, \quad T_{e 13} = T_{e 31}, \quad T_{e 23} = T_{e 32}, \quad \tan \beta, \quad v_S.
\end{aligned} \tag{28}$$

Without special statement, the non-diagonal elements of the parameters are supposed as zero.

A. The processes of $\tau \rightarrow P\mu$

In order to obtain reasonable numerical results, we need to study some sensitive parameters and important mass matrices. Then, to show the numerical results clearly, we will discuss the processes of $\tau \rightarrow Pe$ and $\tau \rightarrow P\mu$ in two subsections. We draw the relation diagrams and scatter diagrams of $Br(\tau \rightarrow Pl)$ with different parameters. After analyzing these graphs and the experimental limits of the branching ratios, reasonable parameter spaces are found to explain LFV.

With the parameters $M_2 = 1 \text{ TeV}$, $m_\nu^2 = 3 \times 10^5 \text{ GeV}^2$, $m_L^2 = 5 \times 10^5 \text{ TeV}^2$, $M_{\nu 12}^2 = M_{\nu 13}^2 = M_{\nu 23}^2 = 100 \text{ GeV}^2$, $M_{L 12}^2 = M_{L 13}^2 = M_{L 23}^2 = 0$, we paint $Br(\tau \rightarrow \mu\pi)$ schematic diagrams affected by different parameters in the Fig.2, where the gray area is current limit on LFV decay $\tau \rightarrow \mu\pi$. Setting $T_\nu = 500 \text{ GeV}$, we plot $Br(\tau \rightarrow \mu\pi)$ versus v_S in the Fig.2(a). The dashed curve corresponds to $\tan \beta = 40$ and the solid line corresponds to $\tan \beta = 20$. We can clearly see that the two lines increase with the increasing v_S in the range of (2000-6000) GeV. The dashed curve is larger than the solid curve. The solid line part as a whole and the dashed line part of $2000 \text{ GeV} < v_S < 4000 \text{ GeV}$ are in the gray area and the dashed line of the rest exceed the gray area.

Supposing $v_S = 4300 \text{ GeV}$, we show $Br(\tau \rightarrow \mu\pi)$ varying with T_ν by the solid curve ($\tan \beta = 10$) and dashed curve ($\tan \beta = 30$) in the Fig.2(b). During the T_ν region (200-800) GeV, both the dashed line and the solid line are increasing functions, and the slope of the dashed line is greater than that of the solid line. The dashed line in the range of 200 GeV to 600 GeV and solid line in the range of 200 GeV to 800 GeV are in the gray area.

Then we analyze the effects of the parameter $\tan\beta$ on branching ratio of $\tau \rightarrow \mu\pi$ and try to find the reasonable ranges. Based on $v_S = 4300$ GeV, the numerical results are shown in the Fig.2(c) by the dashed curve and solid curve corresponding to $T_\nu = 800$ GeV and $T_\nu = 400$ GeV respectively. $Br(\tau \rightarrow \mu\pi)$ varies with $\tan\beta$ in the range from 0.5 to 50. It can be clearly seen that both the solid line and the dashed line have an upward trend. The rising range of the dashed line is greater than that of the solid line. The dashed line in $\tan\beta$ range of 0.5-25 and the solid line in $\tan\beta$ range of 0.5-48 are in the gray area.

$Br(\tau \rightarrow \mu\pi)$ increases as the parameters v_S , T_ν and $\tan\beta$ increase. In the Fig.2(a)(b), the dashed line has a higher slope than the solid line, and the overall direction of the solid line is closer to the experimental upper limit. As $\tan\beta$ goes up, $Br(\tau \rightarrow \mu\pi)$ gets closer to the experimental upper limit. The smaller T_ν is, the closer the whole thing is to the experimental value in the Fig.2(c). All in all, v_S , $\tan\beta$ and T_ν are sensitive parameters that have great impacts on $Br(\tau \rightarrow \mu\pi)$.

Next, we randomly scan the parameters. Some parameters ranges are set as: $\tan\beta$ from 0.5 to 50, v_S from 2000 GeV to 5000 GeV, T_ν from -5000 GeV to 5000 GeV, and $M_{\tilde{\nu}13}^2$ ($M_{\tilde{\nu}32}^2$) from 0 to 10000 GeV². In addition, other parameter spaces are represented in tabular form. Fig.3 is obtained from the parameters shown in the Table III. We use \blacklozenge ($0 < Br(\tau \rightarrow \mu\pi) < 0.1 \times 10^{-8}$), \blacktriangle ($0.1 \times 10^{-8} \leq Br(\tau \rightarrow \mu\pi) < 0.5 \times 10^{-7}$) and \bullet ($0.5 \times 10^{-7} \leq Br(\tau \rightarrow \mu\pi) < 1.1 \times 10^{-7}$) to represent the results in different parameter spaces for the process of $\tau \rightarrow \mu\pi$. The relationship between $\tan\beta$ and $M_{\tilde{\nu}13}^2$ is shown in Fig.3(a). It is obvious that \blacklozenge almost occupy the whole parameter space, and \blacktriangle are mainly distributed in area $0.5 < \tan\beta < 4$ and \bullet in area $4 < \tan\beta < 10$. From the vertical coordinate, \blacktriangle and \bullet concentrate in the range of $M_{\tilde{L}13}^2$ from 4000 GeV² to 10000 GeV².

Fig.3(b) is plotted in the plane of T_ν versus $M_{\tilde{\nu}13}^2$, where \blacklozenge basically exist in the whole coordinate space. \blacktriangle concentrate in $-500 \text{ GeV} < T_\nu < 500 \text{ GeV}$. \bullet are almost symmetrically distributed on both sides of $T_\nu = 0$. \blacktriangle and \bullet concentrate in $4000 \text{ GeV}^2 < M_{\tilde{\nu}13}^2 < 10000 \text{ GeV}^2$ area.

The effect of $M_{\tilde{\nu}12}^2$ and $M_{\tilde{\nu}13}^2$ on $Br(\tau \rightarrow \mu\pi)$ is shown in the Fig.3(c). \blacklozenge are distributed in the lower right area of the connecting line between point ($M_{\tilde{\nu}12}^2 = 0$, $M_{\tilde{\nu}13}^2 = 0$) and point ($M_{\tilde{\nu}12}^2 = 1500 \text{ GeV}^2$, $M_{\tilde{\nu}13}^2 = 10000 \text{ GeV}^2$). On this basis, \blacktriangle and \bullet concentrate in the upper left of the line between point ($M_{\tilde{\nu}12}^2 = 0$, $M_{\tilde{\nu}13}^2 = 0$) and point ($M_{\tilde{\nu}12}^2 = 10000 \text{ GeV}^2$, $M_{\tilde{\nu}13}^2 = 7500 \text{ GeV}^2$), which is obviously layered with the \blacklozenge .

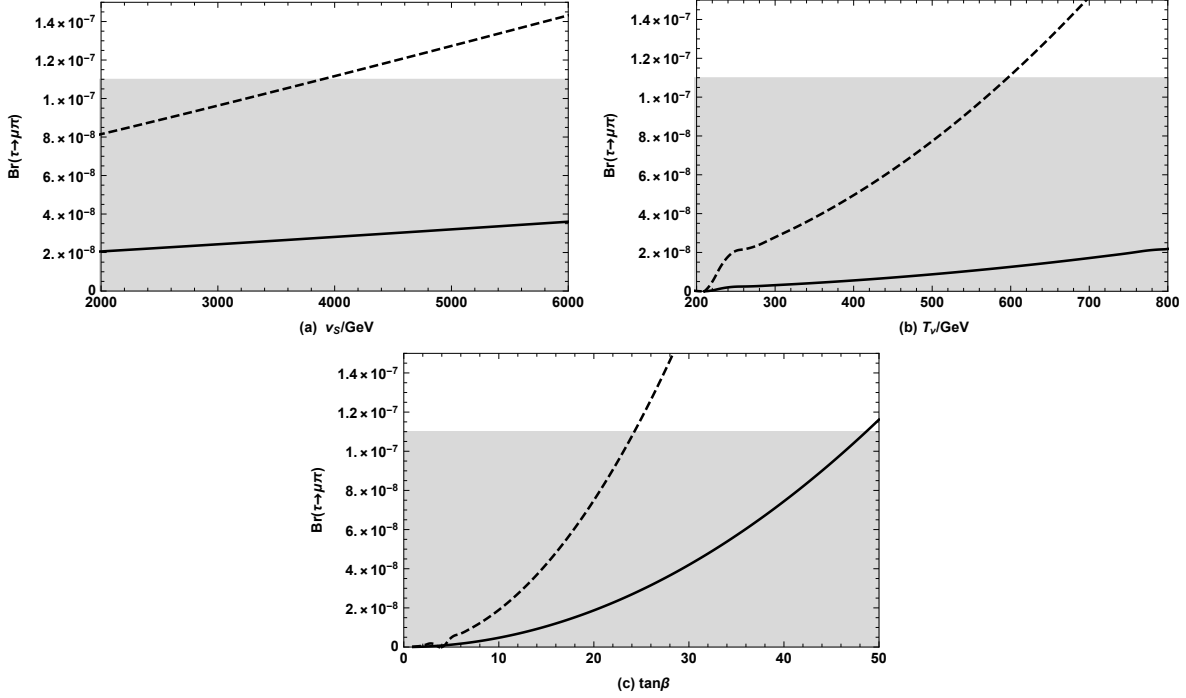


FIG. 2: $Br(\tau \rightarrow \mu\pi)$ schematic diagrams affected by different parameters. The gray area is reasonable value range where $Br(\tau \rightarrow \mu\pi)$ is lower than the upper limit. As $T_\nu = 500$ GeV, the dashed and solid lines in Fig.2(a) correspond to $\tan \beta = 40$ and $\tan \beta = 20$. We set $v_S = 4300$ GeV in Fig.2(b),(c). The dashed line and solid line respectively represent $\tan \beta = 30$ and 10 in Fig.2(b). When $T_\nu = 800$ GeV and 400 GeV, the dashed line and solid line in Fig.2(c) are generated.

Fig.3(d) shows the effect of $\tan \beta$ and T_ν on $Br(\tau \rightarrow \mu\pi)$. \blacklozenge basically occupy the whole value space. The distribution of \blacktriangle is similar to \bullet distribution. They show a downward trend above $T_\nu = 0$ and gradually approach this line. It looks like an increasing function of the relative distribution below $T_\nu = 0$. The difference is that \blacktriangle are closer to $T_\nu = 0$ than \bullet . \blacktriangle exist in $0.5 < \tan \beta < 3$ area where \bullet do not exist.

In order to better study LFV and find a reasonable parameter space in the process of $\tau \rightarrow \mu\eta$, we study the effects of parameters v_S , $\tan \beta$ and T_ν , and draw the scatter diagrams of a certain parameter space in Fig.4. The gray area indicates that it is less than the upper limit of $Br(\tau \rightarrow \mu\eta)$. We suppose the parameters $M_2 = 1$ TeV, $m_{\tilde{\nu}}^2 = 3 \times 10^5$ TeV², $m_L^2 = 5 \times 10^5$ TeV², $M_{L12}^2 = M_{L23}^2 = 10$ GeV² and $M_{\tilde{\nu}12}^2 = M_{\tilde{\nu}23}^2 = M_{\tilde{\nu}13}^2 = 100$ GeV². We draw the solid line ($M_{L13}^2 = 500$ GeV²) and dashed line ($M_{L13}^2 = 2000$ GeV²) in Fig.4(a) to represent the relationship between $\tan \beta$ and $Br(\tau \rightarrow \mu\eta)$ with $v_S = 4300$ GeV and $T_\nu = 500$ GeV.

TABLE III: Scanning parameters for Fig.3

Parameters	Min	Max
$m_{\tilde{L}}^2/\text{GeV}^2$	10^5	10^7
$M_{\tilde{\nu}12}^2/\text{GeV}^2$	0	10^4
T_{e12}/GeV	-3000	3000
T_{e13}/GeV	-3000	3000
T_{e23}/GeV	-3000	3000

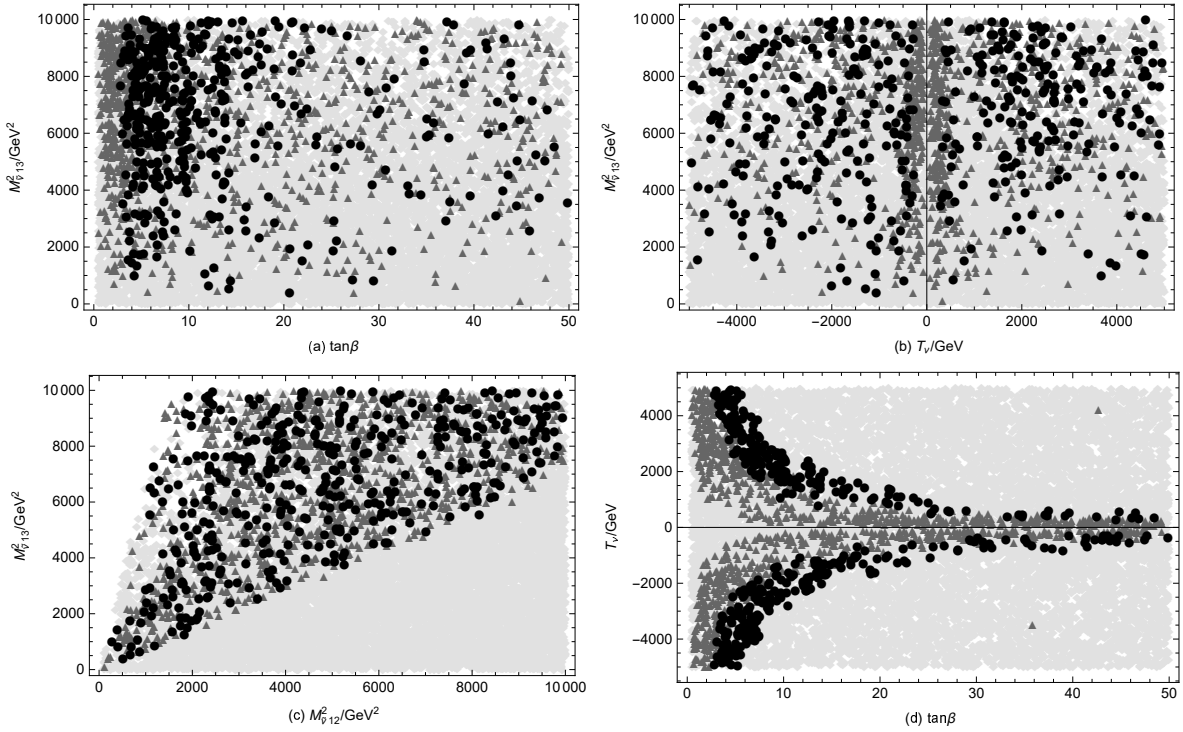


FIG. 3: Under the premise of lower current limit on lepton flavor violating decay $\tau \rightarrow \mu\pi$, reasonable parameter space is selected to scatter points, where \diamond mean the value of $Br(\tau \rightarrow \mu\pi)$ less than 0.1×10^{-8} , \blacktriangle mean $Br(\tau \rightarrow \mu\pi)$ in the range of 0.1×10^{-8} to 0.5×10^{-7} , \bullet show $0.5 \times 10^{-7} \leq Br(\tau \rightarrow \mu\pi) < 1.1 \times 10^{-7}$.

Both dashed line and solid line show an upward trend in $0.5 < \tan\beta < 30$ area, and the increase of solid line is greater than that of dashed line. The solid line of $\tan\beta$ from 0.5 to 12 and the dashed line at $0.5 < \tan\beta < 25$ exist in the gray part.

Adopting $\tan\beta = 9$ and $v_S = 4300$ GeV, we plot the $Br(\tau \rightarrow \mu\eta)$ versus T_ν by the

TABLE IV: Scanning parameters for Fig.4

Parameters	Min	Max
M_2/GeV	500	1500
$M_{\tilde{\nu}12}^2/\text{GeV}^2$	0	10^4
T_{e12}/GeV	0	10^4
T_{e13}/GeV	0	10^4
T_{e23}/GeV	0	10^4

dashed curve ($T_{\nu13} = 200$ GeV) and solid curve ($T_{\nu13} = 50$ GeV) in the Fig.4(b). It can be seen that in the range of 200 GeV to 800 GeV, both the solid line and the dashed line are in the gray area and are growth curves. The difference is that the value of the solid line is larger than that of the dashed line as a whole.

Next, we select v_S in the range of 0-5000 GeV to study its impact on $Br(\tau \rightarrow \mu\eta)$ in Fig.4(c). In addition, we let $\tan\beta = 9$ and $T_\nu = 500$ GeV. The solid line represents $T_{\nu13} = 50$ GeV and the dashed line represents $T_{\nu13} = 200$ GeV. The dashed line and the solid line are rising straight lines and in the gray space. The rising trend of the dashed line is not obvious, but the rising trend of the solid line is obvious. The solid line is larger than the dashed line.

We scatter points according to the parameters given in Table IV to obtain Figs.4(d),(e),(f). These points are divided into \blacklozenge ($0 < Br(\tau \rightarrow \mu\eta) < 1.0 \times 10^{-8}$), \blacktriangle ($1.0 \times 10^{-8} \leq Br(\tau \rightarrow \mu\eta) < 4.0 \times 10^{-8}$) and \bullet ($4.0 \times 10^{-8} \leq Br(\tau \rightarrow \mu\eta) < 6.5 \times 10^{-8}$). In Fig.4(d), we can see that T_ν corresponds to M_{L12}^2 and \blacklozenge concentrate in $-2000 \text{ GeV} < T_\nu < 2000 \text{ GeV}$. \bullet are scattered between $-1500 \text{ GeV} < T_\nu < 1500 \text{ GeV}$, and \blacktriangle mainly concentrate in $-500 \text{ GeV} < T_\nu < 500 \text{ GeV}$ area. We plot T_ν varying with $\tan\beta$ in the Fig.4(e), where the centralized distributions of the three types of points have the same trend. It is almost symmetrical about $T_\nu = 0$. In the $0 < T_\nu < 5000 \text{ GeV}$ region, the subtraction function gradually approaches the $T_\nu = 0$ axis. It is worth noting that in the $0.5 < \tan\beta < 12$ part \blacklozenge , \blacktriangle and \bullet are away from the $T_\nu = 0$ axis in turn. Finally, we analyze the effect from parameters v_S and T_ν in Fig.4(f). All points are almost symmetrically distributed about $T_\nu = 0$ and concentrate in the $-2000 \text{ GeV} < T_\nu < 2000 \text{ GeV}$ region. The farther away from the $T_\nu = 0$ axis, the more sparse the distribution is.

After comparison, it is found that Figs.2(a),(b),(c) are similar to Figs.4(a),(b),(c). In

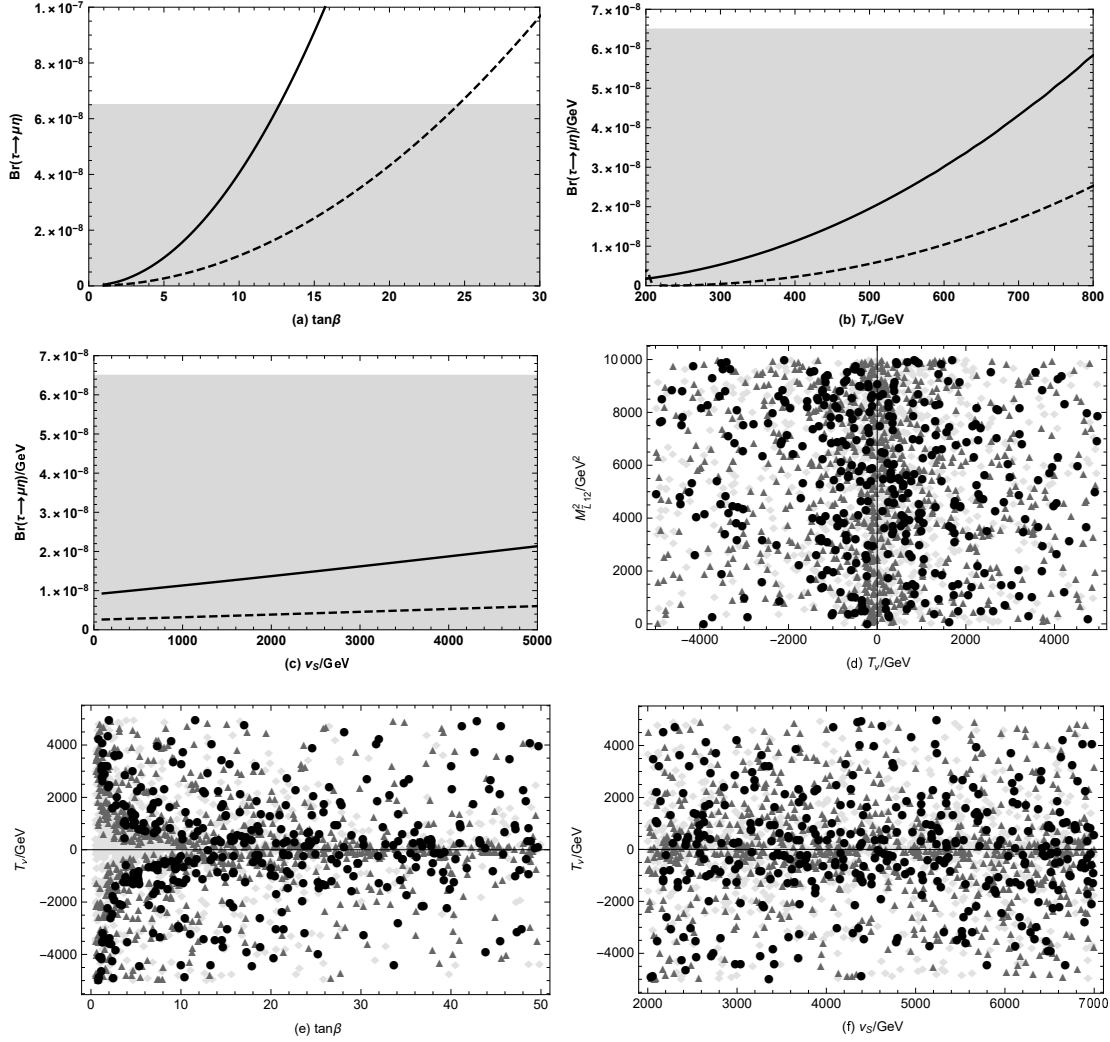


FIG. 4: Based on the experimental upper limit of $Br(\tau \rightarrow \mu\eta)$, the relationship between parameter space and $Br(\tau \rightarrow \mu\eta)$ is studied. As shown in Figs.4(a),(b),(c), the gray area represents the $Br(\tau \rightarrow \mu\eta)$ range below the experimental limit. In Fig.4(a), the solid line corresponds to $M_{L13}^2 = 500 \text{ GeV}^2$ and the dashed line corresponds to $M_{L13}^2 = 2000 \text{ GeV}^2$. The solid and dashed lines in Figs.4(b),(c) refer to $T_{\nu13} = 50 \text{ GeV}$ and 200 GeV . As shown in Figs.4(d),(e),(f), \diamond , \blacktriangle and \bullet represent $0 < Br(\tau \rightarrow \mu\eta) < 1.0 \times 10^{-8}$, $1.0 \times 10^{-8} \leq Br(\tau \rightarrow \mu\eta) < 4.0 \times 10^{-8}$ and $4.0 \times 10^{-8} \leq Br(\tau \rightarrow \mu\eta) < 6.5 \times 10^{-8}$.

order to save time, for the $\tau \rightarrow \mu\eta'$ process we sprinkle the parameters shown in Table V. In the Fig.5, \diamond , \blacktriangle and \bullet indicate that the range of $Br(\tau \rightarrow \mu\eta')$ is $0 - 0.1 \times 10^{-7}$, $0.1 \times 10^{-7} - 0.7 \times 10^{-7}$ and $0.7 \times 10^{-7} - 1.3 \times 10^{-7}$ respectively. Fig.5(a) shows that $\tan\beta$ corresponds to M_{L23}^2 . The distribution of points is more concentrated in $0.5 < \tan\beta < 10$.

TABLE V: Scanning parameters for Fig.5

Parameters	Min	Max
M_2/GeV	500	1500
$M_{\tilde{\nu}12}^2/\text{GeV}^2$	0	10^4
T_{e12}/GeV	0	10^4
T_{e13}/GeV	0	10^4
T_{e23}/GeV	0	10^4

In $0.5 < \tan \beta < 2$ \blacktriangle are more concentrated, and \bullet are mainly in $2 < \tan \beta < 10$. Fig.5(b) is shown in the plane of T_ν versus $M_{\tilde{L}12}^2$, where three types of points are concentrated in $-2000 \text{ GeV} < T_\nu < 2000 \text{ GeV}$. \blacktriangle are mainly in $-50 \text{ GeV} < T_\nu < 50 \text{ GeV}$ and \bullet are mainly in $-1500 \text{ GeV} < T_\nu < -50 \text{ GeV}$ and $50 \text{ GeV} < T_\nu < 1500 \text{ GeV}$. We describe T_ν versus $\tan \beta$ in Fig.5(c). All points are almost symmetrically distributed with $T_\nu = 0$ as the axis. Taking the upper half as an example, the \bullet , \blacktriangle and \blacklozenge like curves that decrease and gradually approach $T_\nu = 0$, and the values decrease in turn. Finally, we give the results in the plane of T_ν and v_S in the Fig.5(d). The points in the parameter space are basically symmetrical about $T_\nu = 0$. The distribution in the region of T_ν from -2000 GeV to 2000 GeV is the most compact and the rest is sparse.

B. The processes of $\tau \rightarrow Pe$

In this subsection, scatter points are in the parameter spaces based on $0.5 < \tan \beta < 50$, $2000 \text{ GeV} < v_S < 7000 \text{ GeV}$, $-5000 \text{ GeV} < T_\nu < 5000 \text{ GeV}$, $M_{\tilde{\nu}12}^2 = M_{\tilde{\nu}13}^2 = M_{\tilde{\nu}23}^2 = M_{\tilde{L}12}^2$ varying from 0 to 500 GeV^2 . other parameter spaces are represented in tabular form.

We analyze $\tau \rightarrow e\pi$, $\tau \rightarrow e\eta$ and $\tau \rightarrow e\eta'$ to study the possibility of lepton flavor violation. Fig.6 is based on the Table VI. The branching ratio of $\tau \rightarrow e\pi$ process is denoted by: \blacklozenge ($0 < Br(\tau \rightarrow e\pi) < 0.1 \times 10^{-9}$), \blacktriangle ($0.1 \times 10^{-9} \leq Br(\tau \rightarrow e\pi) < 3.0 \times 10^{-8}$) and \bullet ($Br(\tau \rightarrow e\pi)$ from 3.0×10^{-8} to 8.0×10^{-8}). The Fig.6(a) shows contribution from $\tan \beta$ and $M_{\tilde{L}13}^2$. All points concentrate in the lower left corner and near the two coordinate axes. The \bullet as a whole is a subtraction function close to the two allowable standard axes and is located on the outermost side of the whole region. The general trend of \blacktriangle in the black area and the middle of the two coordinate axes is also downward. In Fig.6(b), we analyze the effects of T_ν

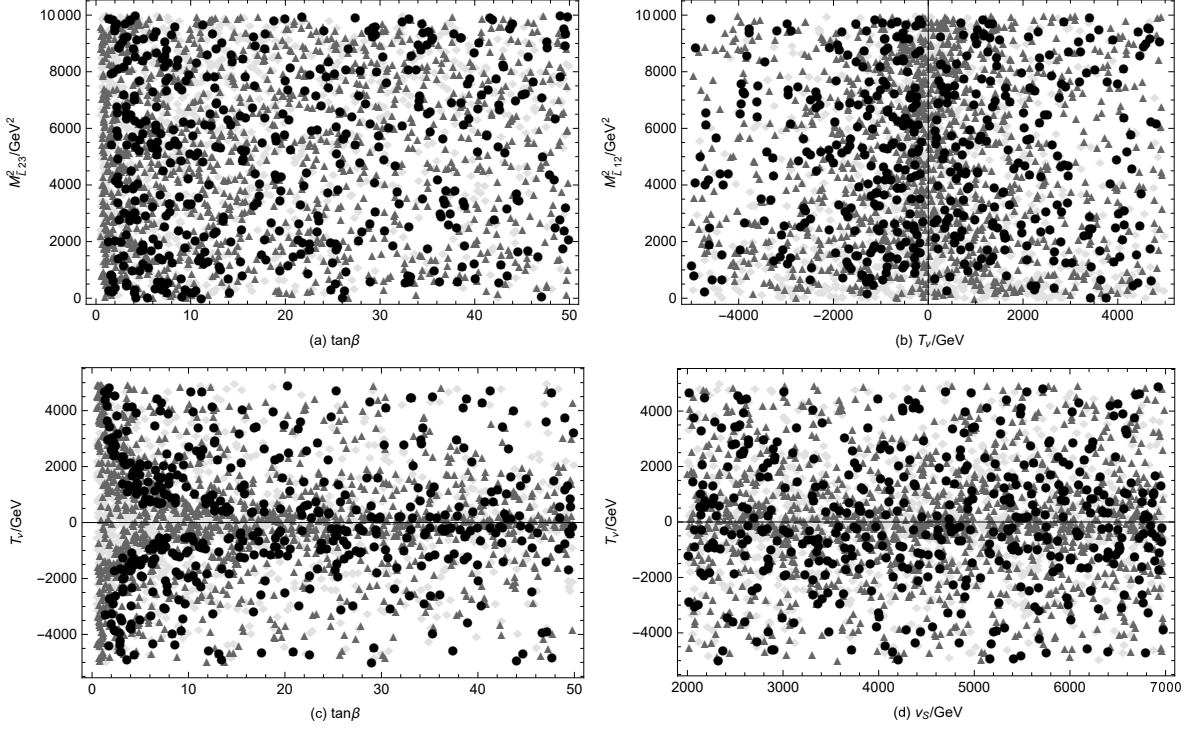


FIG. 5: Scatter points in an area smaller than the upper limit of $Br(\tau \rightarrow \mu\eta')$. \blacklozenge represent $0 < Br(\tau \rightarrow \mu\eta') < 0.1 \times 10^{-7}$, \blacktriangle represent $0.1 \times 10^{-7} \leq Br(\tau \rightarrow \mu\eta') < 0.7 \times 10^{-7}$ and $0.7 \times 10^{-7} \leq Br(\tau \rightarrow \mu\eta') < 1.3 \times 10^{-7}$ are represented by \bullet .

TABLE VI: Scanning parameters for Fig.6

Parameters	Min	Max
M_2/GeV	500	1500
$m_{\tilde{\nu}}^2/\text{GeV}^2$	1000	5×10^5
M_{L13}^2/GeV^2	0	200

and M_{L13}^2 on $Br(\tau \rightarrow e\pi)$. Most of the three types points are at $0 < M_{L13}^2 < 50 \text{ GeV}^2$. There are obvious stratification: \bullet is greater than \blacktriangle and \blacktriangle is greater than \blacklozenge . In the Fig.6(c) with two axes M_{L12}^2 versus M_{L13}^2 , most of the points concentrate in $0 < M_{L13}^2 < 50 \text{ GeV}^2$ and most of \blacklozenge are in $0 < M_{L13}^2 < 10 \text{ GeV}^2$. The effect from M_{L12}^2 and M_{L13}^2 is shown in Fig.6(d), where the points distribute at the lower right of the connecting line between $(M_{L12}^2=0, M_{L13}^2=0)$ and $(M_{L12}^2=200 \text{ GeV}^2, M_{L13}^2=200 \text{ GeV}^2)$ and concentrate in the range of M_{L13}^2 from 0 to 50 GeV^2 . \blacktriangle and \bullet are obviously layered and \blacktriangle concentrate below $M_{L13}^2 = 10 \text{ GeV}^2$.

Next, we scatter points on $\tau \rightarrow e\eta$ in Fig.7 with the parameters in the Table VII. \blacklozenge , \blacktriangle and

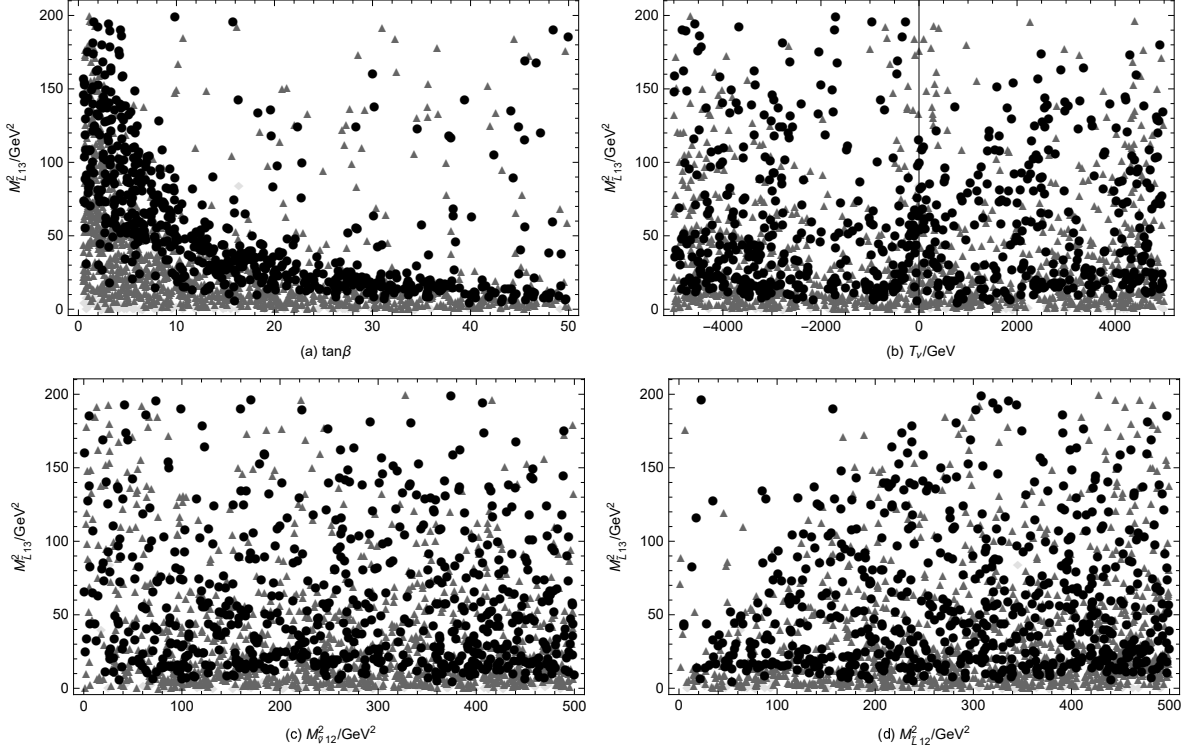


FIG. 6: For the scatter diagrams of the parameters below the experimental limit $Br(\tau \rightarrow e\pi)$, different points represent the different ranges of $Br(\tau \rightarrow e\pi)$. \diamond represent less than 0.1×10^{-9} , \blacktriangle represent the range of 0.1×10^{-9} to 3.0×10^{-8} , and \bullet represent the range of 3.0×10^{-8} to 8.0×10^{-8} .

\bullet indicate the range $0 < Br(\tau \rightarrow e\eta) < 0.1 \times 10^{-8}$, $0.1 \times 10^{-8} \leq Br(\tau \rightarrow e\eta) < 5.0 \times 10^{-8}$ and $5.0 \times 10^{-8} \leq Br(\tau \rightarrow e\eta) < 9.2 \times 10^{-8}$ respectively. In Fig.7(a), we show the points in the plane of $\tan\beta$ and M_{L23}^2 . The three types of points have the same downward trend and gradually approach $M_{L23}^2 = 0$ and $\tan\beta=0$. \bullet are on the outermost side of the whole area. \blacktriangle are in the middle and \diamond are on the innermost side. We show $\tan\beta$ versus T_ν in Fig.7(b). The whole diagram is almost symmetrical about $T_\nu = 0$ and concentrate in area $0 < \tan\beta < 25$. \blacktriangle are mainly in $0.5 < \tan\beta < 5$ and on both sides of the $T_\nu = 0$ axis. Next, in Fig.7(c), we show the relationship between T_ν and M_{L23}^2 . Most of the points are in region of M_{L23}^2 from 0 to 250 GeV^2 and near axis $T_\nu = 0$. \diamond mainly concentrate near $T_\nu = 0$. Finally, we analyze the impact of $\tan\beta$ and M_{L12}^2 on $Br(\tau \rightarrow \mu\eta)$ in Fig.7(d). \blacktriangle mainly concentrate in $\tan\beta$ range from 0.5 to 5 and \bullet concentrate in area $5 < \tan\beta < 20$.

The drawing of Fig.8 is similar to the previous one. We draw the process of $\tau \rightarrow e\eta'$ according to table VIII. \diamond indicate that the value of $Br(\tau \rightarrow e\eta')$ is from 0 to 2.0×10^{-8} , \blacktriangle

TABLE VII: Scanning parameters for Fig.7

Parameters	Min	Max
$m_{\tilde{\nu}}^2/\text{GeV}^2$	1000	5×10^5
M_{L23}^2/GeV^2	0	500
M_{L13}^2/GeV^2	0	100

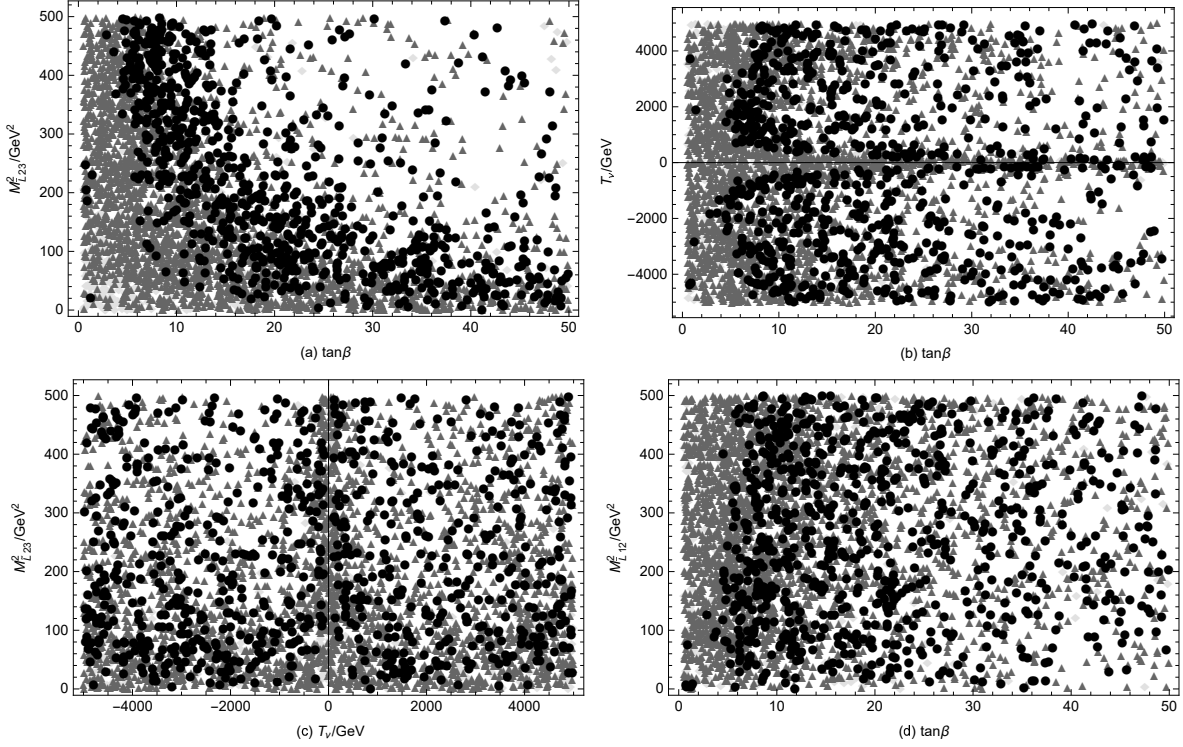


FIG. 7: Scatter points on the parameters under the limit of $Br(\tau \rightarrow e\eta)$ less than 9.2×10^{-8} , in which \diamond , \blacktriangle and \bullet represent $0 < Br(\tau \rightarrow e\eta) < 0.1 \times 10^{-8}$, $0.1 \times 10^{-8} \leq Br(\tau \rightarrow e\eta) < 5.0 \times 10^{-8}$ and $5.0 \times 10^{-8} \leq Br(\tau \rightarrow e\eta) < 9.2 \times 10^{-8}$ respectively.

indicate a range of $2.0 \times 10^{-8} \leq Br(\tau \rightarrow \mu\eta') < 9.0 \times 10^{-8}$ and \bullet are $9.0 \times 10^{-8} \leq Br(\tau \rightarrow \mu\eta') < 1.6 \times 10^{-7}$. We describe the effect of M_{L23}^2 and $\tan\beta$ on $Br(\tau \rightarrow e\eta')$ in Fig.8(a). We can easily see that \diamond , \blacktriangle and \bullet all have the same downward trend, which are distributed in the lower left part, and the values become larger in turn. We show T_ν versus M_{L23}^2 in the Fig.8(b). The points mainly concentrate in $0 < M_{L23}^2 < 200 \text{ GeV}^2$ and are generally symmetrical about $T_\nu = 0$. Numerically, \bullet is the largest, followed by \diamond and the smallest is \blacktriangle . It should not be ignored that on both sides of $T_\nu = 0$, there are \diamond , \blacktriangle and \bullet from inside

TABLE VIII: Scanning parameters for Fig.8

Parameters	Min	Max
$m_{\tilde{\nu}}^2/\text{GeV}^2$	1000	5×10^5
M_{L23}^2/GeV^2	0	500
M_{L13}^2/GeV^2	0	50

to outside. Next, we draw the relationship between T_ν and $\tan\beta$ in Fig.8(c). The whole picture is almost symmetrical about $T_\nu = 0$. \blacklozenge are in the range of $\tan\beta$ from 0.5 to 3, \blacktriangle is in the range of $3 < \tan\beta < 7$, and most of the rest are distributed with \bullet . In order to study $\tan\beta$ and $M_{\tilde{\nu}13}^2$ more intuitively, we draw Fig.8(d) with \blacklozenge at $0 < \tan\beta < 3$, \blacktriangle at $3 < \tan\beta < 7$, \bullet at $7 < \tan\beta < 25$.

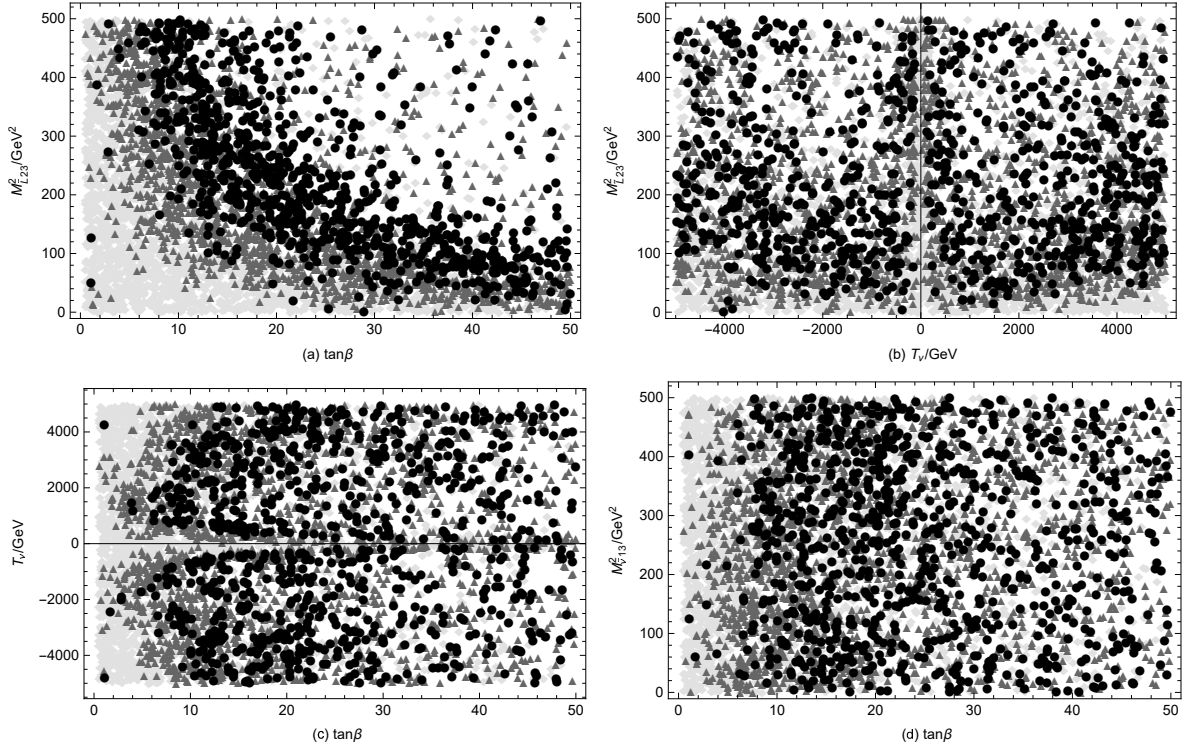


FIG. 8: Considering the limit of $Br(\tau \rightarrow e\eta')$, the diagrams are plotted, where \blacklozenge represent $0 < Br(\tau \rightarrow \mu\eta') < 2.0 \times 10^{-8}$, \blacktriangle represent $2.0 \times 10^{-8} \leq Br(\tau \rightarrow \mu\eta') < 9.0 \times 10^{-8}$ and $9.0 \times 10^{-8} \leq Br(\tau \rightarrow \mu\eta') < 1.6 \times 10^{-7}$ are represented by \bullet .

V. DISCUSSION AND CONCLUSION

The $U(1)_X$ SSM is the $U(1)$ extension of MSSM, and its local gauge group is $SU(3)_C \times SU(2)_L \times U(1)_Y \times U(1)_X$. Comparing with MSSM, $U(1)_X$ SSM has new superfields including righ-handed neutrinos and three Higgs superfields $\hat{\eta}$, $\hat{\bar{\eta}}$, \hat{S} , which leads to several advantages as introduced in the introduction. This model possesses more LFV sources, which can give considerable contributions to the LFV processes $\tau \rightarrow Pl$. We take into account the one loop diagrams which include self-energy diagram, triangle diagram and box diagram. In the numerical calculation, we scan large parameter spaces and make a rich numerical results. As a result, many diagrams of the numerical results are plotted.

In this work, taking into account the constraints from the upper limits on LFV branching ratios of $\tau \rightarrow Pl$ at 90% C.L., we use the effective Lagrangian method to calculate and analyze the LFV decays $\tau \rightarrow Pl$ in the framework of the $U(1)_X$ SSM model. We scan a large number of parameters to find the possibility of LFV. After comparison and analysis, $\tan \beta$, T_ν , $M_{\nu 13}^2$, $M_{L 23}^2$ and $M_{L 13}^2$ are sensitive parameters that have great impacts on the results. $M_{L 12}^2$, v_S and $M_{\nu 12}^2$ are insensitive parameters. In the whole, the non-diagonal elements which correspond to the generations of the initial lepton and final lepton are main sensitive parameters and LFV sources. Most parameters can break the upper limit of the experiment and provide new ideas for finding NP.

Acknowledgments

This work is supported by National Natural Science Foundation of China (NNSFC) (No. 11535002, No. 11705045), Natural Science Foundation of Hebei Province (A2020201002). Post-graduate's Innovation Fund Project of Hebei University.

Appendix A: mass matrix

The mass matrix for slepton with the basis $(\tilde{e}_L, \tilde{e}_R)$ is diagonalized by Z^E through the formula $Z^E m_{\tilde{e}}^2 Z^{E,\dagger} = m_{2,\tilde{e}}^{diag}$,

$$m_{\tilde{e}}^2 = \begin{pmatrix} m_{\tilde{e}_L \tilde{e}_L^*} & \frac{1}{2} \left(\sqrt{2} v_d T_e^\dagger - v_u \left(\lambda_H v_S + \sqrt{2} \mu \right) Y_e^\dagger \right) \\ \frac{1}{2} \left(\sqrt{2} v_d T_e - v_u Y_e \left(\sqrt{2} \mu^* + v_S \lambda_H^* \right) \right) & m_{\tilde{e}_R \tilde{e}_R^*} \end{pmatrix}, \quad (\text{A1})$$

$$m_{\tilde{e}_L \tilde{e}_L^*} = M_L^2 + \frac{1}{8} \left((g_1^2 + g_{YX}^2 + g_{YX} g_X - g_2^2) (v_d^2 - v_u^2) + 2 g_{YX} g_X (v_\eta^2 - v_{\bar{\eta}}^2) \right) + \frac{1}{2} v_d^2 Y_e^\dagger Y_e,$$

$$m_{\tilde{e}_R \tilde{e}_R^*} = M_E^2 - \frac{1}{8} \left([2(g_1^2 + g_{YX}^2) + 3g_{YX}g_X + g_X^2](v_d^2 - v_u^2) + (4g_{YX}g_X + 2g_X^2)(v_\eta^2 - v_{\tilde{\eta}}^2) \right) + \frac{1}{2} v_d^2 Y_e Y_e^\dagger. \quad (\text{A2})$$

The mass matrix for neutralino in the basis $(\lambda_{\tilde{B}}, \tilde{W}^0, \tilde{H}_d^0, \tilde{H}_u^0, \lambda_{\tilde{X}}, \tilde{\eta}, \tilde{\tilde{\eta}}, \tilde{s})$ is

$$m_{\tilde{\chi}^0} = \begin{pmatrix} M_1 & 0 & -\frac{g_1}{2}v_d & \frac{g_1}{2}v_u & M_{BB'} & 0 & 0 & 0 \\ 0 & M_2 & \frac{1}{2}g_2v_d & -\frac{1}{2}g_2v_u & 0 & 0 & 0 & 0 \\ -\frac{g_1}{2}v_d & \frac{1}{2}g_2v_d & 0 & m_{\tilde{H}_d^0 \tilde{H}_u^0} & m_{\tilde{H}_d^0 \lambda_{\tilde{X}}} & 0 & 0 & -\frac{\lambda_H v_u}{\sqrt{2}} \\ \frac{g_1}{2}v_u & -\frac{1}{2}g_2v_u & m_{\tilde{H}_d^0 \tilde{H}_u^0} & 0 & m_{\tilde{H}_u^0 \lambda_{\tilde{X}}} & 0 & 0 & -\frac{\lambda_H v_d}{\sqrt{2}} \\ M_{BB'} & 0 & m_{\tilde{H}_d^0 \lambda_{\tilde{X}}} & m_{\tilde{H}_u^0 \lambda_{\tilde{X}}} & M_{BL} & -g_X v_\eta & g_X v_{\tilde{\eta}} & 0 \\ 0 & 0 & 0 & 0 & -g_X v_\eta & 0 & \frac{1}{\sqrt{2}}\lambda_C v_S & \frac{1}{\sqrt{2}}\lambda_C v_{\tilde{\eta}} \\ 0 & 0 & 0 & 0 & g_X v_{\tilde{\eta}} & \frac{1}{\sqrt{2}}\lambda_C v_S & 0 & \frac{1}{\sqrt{2}}\lambda_C v_\eta \\ 0 & 0 & -\frac{\lambda_H v_u}{\sqrt{2}} & -\frac{\lambda_H v_d}{\sqrt{2}} & 0 & \frac{1}{\sqrt{2}}\lambda_C v_{\tilde{\eta}} & \frac{1}{\sqrt{2}}\lambda_C v_\eta & m_{\tilde{s}\tilde{s}} \end{pmatrix}, \quad (\text{A3})$$

$$\begin{aligned} m_{\tilde{H}_d^0 \tilde{H}_u^0} &= -\frac{1}{\sqrt{2}}\lambda_H v_S - \mu, & m_{\tilde{H}_d^0 \lambda_{\tilde{X}}} &= -\frac{1}{2}(g_{YX} + g_X)v_d, \\ m_{\tilde{H}_u^0 \lambda_{\tilde{X}}} &= \frac{1}{2}(g_{YX} + g_X)v_u, & m_{\tilde{s}\tilde{s}} &= 2M_S + \sqrt{2}\kappa v_S. \end{aligned} \quad (\text{A4})$$

This matrix is diagonalized by Z^N

$$Z^{N*} m_{\tilde{\chi}^0} Z^{N\dagger} = m_{\tilde{\chi}^0}^{diag}. \quad (\text{A5})$$

-
- [1] K. Abe et al. (T2K Collaboration), Phys. Rev. Lett. **107** (2011) 041801; J. Ahn et al. (RENO Collaboration), Phys. Rev. Lett. **108** (2012) 191802; F. An et al. (DAYABAY Collaboration), Phys. Rev. Lett. **108** (2012) 171803.
 - [2] S. T. Petcov, Sov. J. Nucl. Phys. **25** (1977) 340.
 - [3] F. Staub, [arXiv: 0806.0538].
 - [4] F. Staub, Comput. Phys. Commun. **185** (2014) 1773 [arXiv: 1309. 7223].
 - [5] F. Staub, Adv. High Energy Phys. **2015** (2015) 840780 [arXiv: 1503. 04200].
 - [6] J. Rosiek, Phys. Rev. D **41** (1990) 3464; [arXiv:hep-ph/9511250v3].

- [7] CMS collaboration, Phys. Lett. B **716** (2012) 30; ATLAS collaboration, Phys. Lett. B **716** (2012) 1.
- [8] U. Ellwanger, C. Hugonie, A.M. Teixeira, Phys. Rep. **496** (2010) 1-77, [arXiv: 0910.1785] [hep-ph].
- [9] W. J. Li, Y. D. Yang and X. D. Zhang, Phys. Rev. D **73** (2006) 073005.
- [10] S. Kanemura, T. Ota and K. Tsumura, Phys. Rev. D **73** (2006) 016006.
- [11] T. Goto, Y. Okada and Y. Yamamoto, Phys. Rev. D **83** (2011) 053011.
- [12] C. X. Yue, L. H. Wang and W. Ma, Phys. Rev. D **74** (2006) 115018.
- [13] M. Sher, Phys. Rev. D **66** (2002) 057301.
- [14] T. Fukuyama, A. Ilakovac and T. Kikuchi, Eur. Phys. J. C **125** (2008) 56.
- [15] C. H. Chen and C. Q. Geng, Phys. Rev. D **74** (2006) 035010.
- [16] J. P. Saha and A. Kundu, Phys. Rev. D **66** (2002) 054021.
- [17] K. S. Sun , T. Guo and W. Li, Eur. Phys. J. C **80** (2020) 1167.
- [18] Particle Data Group, Prog. Theor. Exp. Phys. **2020** (2020) 083C01.
- [19] B. Yan, S. M. Zhao and T. F. Feng 2011.08533 [hep-ph].
- [20] S.M. Zhao and T.F. Feng, JHEP **02** (2020) 130.
- [21] S.M. Zhao, L.H. Su and X.X. Dong, 2107.03571 [hep-ph].
- [22] M. Carena, J.R. Espinosa, C.E.M. Wagner, et al., Phys. Lett. B **355** (1995) 209 [hep-ph/9504316].
- [23] M. Carena, S. Gori, N.R. Shah, et al., JHEP **1203** (2012) 014 [arXiv: 1112. 3336].
- [24] G. Belanger, J.D. Silva, H.M. Tran, Phys. Rev. D **95** (2017) 115017 [arXiv: 1703. 03275].
- [25] V. Barger, P.F. Perez, S. Spinner, Phys. Rev. Lett. **102** (2009) 181802 [arXiv: 0812. 3661].
- [26] P.H. Chankowski, S. Pokorski, J. Wagner, Eur. Phys. J. C **47** (2006) 187 [hep-ph/0601097].
- [27] J.L. Yang, T.F. Feng, S.M. Zhao, et al., Eur. Phys. J. C **78** (2018) 714 [arXiv: 1803. 09904].
- [28] L.H. Su and S.M. Zhao, Eur. Phys. J. C **81** (2021) 433.
- [29] S.M. Zhao, G.Z.Ning and J.J. Feng, Nucl. Phys. B **969** (2021) 115469.
- [30] W. Porod and F. Staub, A. Vicente, Eur. Phys. J. C **74** (2014) 2992.
- [31] E. Arganda, M.J. Herrero and J. Portoles, J. High Energy Phys. **79** (2008) 0806.
- [32] CMS Collaboration, Phys. Lett. B **716** (2012) 30.
- [33] A TLAS Collaboration, Phys. Lett. B **716** (2012) 1.
- [34] G. Aad et al., (ATLAS Collaboration), Phys. Lett. B **796** (2019) 68-87 [arXiv:hep

ex/1903.06248].

- [35] G. Cacciapaglia, C. Csaki, G. Marandella, et al., Phys. Rev. D **74** (2006) 033011 [hep-ph/0604111].
- [36] M. Carena, A. Daleo, B. A. Dobrescu, et al., Phys. Rev. D **70** (2004) 093009 [hep-ph/0408098].
- [37] L. Basso, Adv. High Energy Phys. **2015** (2015) 980687 [arXiv: 1504. 05328].